



*Citation for published version:*

Wright, CJ, Hindley, NP & Mitchell, NJ 2016, 'Combining AIRS and MLS observations for three-dimensional gravity wave measurement', *Geophysical Research Letters*, vol. 43, no. 2, pp. 884-893.  
<https://doi.org/10.1002/grl.v43.2>

*DOI:*

[10.1002/grl.v43.2](https://doi.org/10.1002/grl.v43.2)

*Publication date:*

2016

*Document Version*

Publisher's PDF, also known as Version of record

[Link to publication](#)

*Publisher Rights*

CC BY

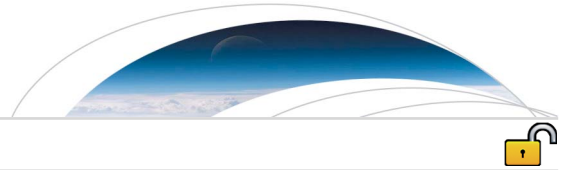
## University of Bath

**General rights**

Copyright and moral rights for the publications made accessible in the public portal are retained by the authors and/or other copyright owners and it is a condition of accessing publications that users recognise and abide by the legal requirements associated with these rights.

**Take down policy**

If you believe that this document breaches copyright please contact us providing details, and we will remove access to the work immediately and investigate your claim.



## RESEARCH LETTER

10.1002/2015GL067233

## Key Points:

- We present a new method of detecting gravity waves in 3-D from satellite data
- This method allows the computation of net momentum fluxes, i.e., after directional cancelation
- Our observational filter lies in the highest-momentum flux part of the spectrum

## Correspondence to:

C. J. Wright,  
corwin.wright@trinity.oxon.org

## Citation:

Wright, C. J., N. P. Hindley, and N. J. Mitchell (2016), Combining AIRS and MLS observations for three-dimensional gravity wave measurement, *Geophys. Res. Lett.*, 43, 884–893, doi:10.1002/2015GL067233.

Received 30 NOV 2015

Accepted 28 DEC 2015

Accepted article online 1 JAN 2016

Published online 23 JAN 2016

©2016. The Authors.

This is an open access article under the terms of the Creative Commons Attribution License, which permits use, distribution and reproduction in any medium, provided the original work is properly cited.

## Combining AIRS and MLS observations for three-dimensional gravity wave measurement

Corwin J. Wright<sup>1</sup>, Neil P. Hindley<sup>1</sup>, and Nicholas J. Mitchell<sup>1</sup>

<sup>1</sup>Centre for Space, Atmospheric and Oceanic Science, University of Bath, Bath, UK

**Abstract** Gravity waves play a critical role in transporting energy and momentum between the troposphere, stratosphere, and mesosphere. Satellite measurements provide a powerful tool to investigate these waves across the globe. However, many present methods cannot yield reliable estimates of wave momentum fluxes or the directions of these fluxes. Here we present a new method which addresses this problem by combining observations from Atmospheric Infrared Sounder (AIRS) and Microwave Limb Sounder (MLS) in three dimensions. The method allows direct estimation of horizontal and vertical wavelengths as well as wave amplitude. This in turn allows estimation of both wave momentum flux and the full 3-D direction of propagation, crucially including the horizontal direction. The method thus allows separation of the data into, for example, eastward and westward momentum fluxes, allowing estimation of the net atmospheric forcing due to these waves. We illustrate this method with a proof-of-concept study over the Andes, arguably the largest source of gravity waves in the world. We further critically assess the advantages and disadvantages of our method. Our study highlights the importance of the difference between net and absolute measures of momentum flux.

### 1. Introduction

Gravity waves (GWs) are atmospheric waves generated by processes including wind flow over mountains, jet stream instabilities, and meteorological sources including weather systems and convection. They transport energy and momentum by coupling and connecting the atmospheric layers. They dominate the driving of the atmospheric flow at all altitudes above the troposphere. Understanding GWs, and their fluxes of energy and momentum, is therefore vital for both numerical weather prediction and climate modeling [Lindzen, 1981; Holton, 1983; Fritts, 1984; Andrews et al., 1987; Fritts and Alexander, 2003; Alexander et al., 2010].

GWs can be directly observed by a broad range of techniques, included ground-based radar and lidar, and in situ tracer balloons and radiosondes. Such measurements are often intrinsically restricted to specific locations. This leads to biases in our measurements and significantly limits coverage in remote regions such as the open ocean. To characterize global GW effects in a comprehensive and balanced way, only satellite measurements provide the necessary geographic range.

Over the last two decades, advances in satellite technology [e.g., Eckermann and Preusse, 1999; Alexander and Barnett, 2007; Barnett et al., 2008; Yan et al., 2010] and analytical methods [e.g., Wu and Waters, 1996; Preusse et al., 2002; Ern et al., 2004; Alexander et al., 2008] have permitted the characterization of GWs from satellite temperature observations. However, these measurements have been limited to either vertical (limb-sounding) or horizontal (nadir-sounding) 2-D along-track planes. Since these measurements are also near instantaneous due to the high velocity of satellites, this prevents us from measuring wave directions, and thus estimating net (i.e., after directional cancelation of multiple waves) wave fluxes. Such 2-D data also lead to persistent and major underestimates of GW horizontal wave number for limb sounders [Alexander, 2015] and to a lack of any direct vertical wave number information for nadir sounders [Alexander et al., 2009].

While no single existing instrument can consistently observe GWs in 3-D, combined measurements from collocated instruments can do so. In one approach, Alexander and Teitelbaum [2011] examined spatial coincidences between the nadir-sensing Atmospheric Infrared Sounder (AIRS) and the limb-sounding High Resolution Dynamics Limb Sounder (HIRDLS), using the Weather Research Forecasting (WRF) model to couple between their different overpass times. However, due to their shared orbit and very different view directions, these measurements never coincide temporally except poleward of 80°N, making direct use of them in combination impossible without model support.

In another approach, *Wang and Alexander* [2010] and *Faber et al.* [2013] used temporally and spatially closely located (hereafter simply “colocated”) triplets of Constellation Observing System for Mesosphere, Ionosphere and Climate (COSMIC) GPS-RO profiles. *Alexander* [2015] modified this method to take advantage of additional HIRDLS profiles, greatly expanding the number of useful colocations. However, such coincidences are still rare. For example, HIRDLS and COSMIC measurements coincided only  $\sim 10,000$  times (within 900 s and 180 km) during the 3 year HIRDLS mission [*Wright et al.*, 2011]. COSMIC-only triplets are substantially rarer than this [*Alexander*, 2015]. Furthermore, this method cannot directly measure horizontal wavelength but, instead, infers it from vertical phase changes between profiles. This is highly dependent on phase measurement accuracy, which particularly for short wavelength waves at small horizontal profile separations, can lead to fractionally very large errors [*Wright*, 2010; *Hindley et al.*, 2015]. Such errors are highly significant in estimates of momentum flux (MF), a key quantity governing how GWs drive the upper atmosphere.

Here we present a new method combining data from AIRS and the Microwave Limb Sounder (MLS). This method enables global measurements of momentum flux to be made with unprecedented precision and with greatly improved temporal and spatial coverage.

A critical advantage of this instrument pairing is that the two instruments share an orbit, thus providing access to over 1,000,000 colocated measurements (recorded over 12 years to date). This number of colocations is defined in terms of AIRS granules and corresponds to a value of around an order of magnitude more when defined in terms of MLS profiles. The 1,000,000 value is 2 orders of magnitude more than HIRDLS-COSMIC triplets and is (at time of writing) increasing by 90,000 per year while the two instruments continue to operate. All observations from these instruments have perfect geographic colocation within 10 min, the vast majority within 90 s.

AIRS/MLS combined observations have further advantages. They have finer horizontal resolution than any limb-sounder-only method, allowing access to the short horizontal/long vertical wavelengths vital for momentum flux transport, which are inaccessible to triplet methods. Further, they can also directly measure wavelengths, rather than infer them from phase changes. Finally, they better constrain the 3-D planes of the waves, allowing us to compute directional and hence net, momentum fluxes, under the single assumption of vertical wave ascent (section 5.1.4).

Section 2 describes the data. Section 3 illustrates a case study over the Andes in May 2008 and outlines our new method for characterizing observed waves. Section 4 applies this to a larger set of observations in the same region. Section 5 describes remaining limitations in our proof-of-concept method before section 6 outlines some brief conclusions.

## 2. AIRS, MLS, and the A-Train

AIRS and MLS are part of the A-Train. This is a satellite constellation in Sun-synchronous polar orbit, with an ascending-node equator-crossing time of 1.30 P.M. The constellation completes 14.55 orbits per day with a 16 day repeat cycle. The A-Train consist of a diverse range of instruments aboard many independent spacecraft and is designed to collect coincident measurements.

### 2.1. AIRS

Launched on the 4 May 2002, AIRS is an 2378-channel infrared nadir sounder aboard NASA/Aqua. AIRS scans across track from  $+49.5^\circ$  to  $-49.5^\circ$  off axis, measuring a continuous swath of radiances. The data are processed as 90 parallel scan tracks, with horizontal resolution varying from  $\sim 13.5$  km  $\times$  13.5 km at nadir to 41 km  $\times$  21.4 km at track edge, and stored in 135 row “granules” corresponding to 6 min of data [*Aumann et al.*, 2003; *Chahine et al.*, 2006; *Olsen et al.*, 2007].

We use AIRS L1 (v5) radiances; these have considerably higher horizontal resolution than the AIRS L2 temperature product and are consequently more useful for studying small-scale features. They also preserve wave features in the vertical, which the standard AIRS L2 product suppresses [*Alexander and Barnett*, 2007; *Hoffmann and Alexander*, 2009].

Specifically, we use brightness temperatures computed from channel 75 radiances as

$$T_B = \frac{hck_r}{k_B} \left( \ln \left( \frac{2hc^2k_r^3}{R} + 1 \right) \right)^{-1}, \quad (1)$$

where  $h$  is Planck's constant,  $c$  the speed of light,  $k_B$  Boltzmann's constant,  $k_r$  the radiance channel's wave number, and  $R$  the radiance. Channel 75 is vertically centered at 2.5 hPa ( $\sim 42$  km) and has a deep weighting function with a full width at half maximum (FWHM) of  $\sim 14$  km [illustrated in Figure 1 of Wright *et al.*, 2015a]. Our analysis is generalizable to other AIRS channels.

We detrend  $T_b$  across track with a fourth order polynomial [Alexander and Barnett, 2007], leaving perturbations  $T'_A$  around the local mean. These data are suited to measuring GWs with short horizontal wavelength and large vertical wavelengths. Specifically, XT detectable horizontal wavelengths are defined by the polynomial detrending, with 90% and 50% sensitivity for wavelengths up to 800 and 1200 km, respectively [see Figure 5 of Hoffmann *et al.*, 2014 for details]. In the AT direction, considerably longer horizontal wavelengths can be detected in principle but may be discarded by the detrending procedure if they cover a large proportion of the swath and closely parallel the AT axis.

## 2.2. MLS

MLS flies aboard NASA/Aura. It is designed to measure a wide range of physical and chemical quantities, including temperature [Schoeberl *et al.*, 2006; Waters *et al.*, 2006].

We use v3.3/3.4 (hereafter simply v3.3) of the MLS-Aura L2 product. V3.3 temperature covers the range 261 hPa–0.001 hPa ( $\sim 10$ –100 km), with a stratospheric precision  $\sim 0.6$  K up to at least the 0.316 hPa level [Livesey *et al.*, 2013]. Large-scale zonal structure is removed by fitting and removing sine waves of planetary mode 0–7 in temperature from the global data set for that day in  $5^\circ$  latitude bands, leaving temperature perturbations  $T'_M$ .

Along-track resolution is  $\sim 170$  km from 261 hPa to 0.1 hPa, and across-track resolution, defined by the 118 GHz channel field of view, is  $\sim 12$  km in the stratosphere. Vertical resolution varies with height, from 3.6 km to 6 km (as illustrated on page 148 of Livesey *et al.* [2013]). While this is much coarser than instruments typically used to measure GWs such as HIRDLS ( $\sim 1$  km), COSMIC ( $\sim 1.5$  km), and SABER ( $\sim 2$  km), it is substantially finer than the vertical resolution of AIRS and thus can vertically resolve any wave visible to AIRS.

## 2.3. Colocated Measurements

AIRS observes in the nadir of Aqua, while MLS observes the Earth's limb ahead of Aura  $66^\circ$  off track. From 2004 to 2007 Aura orbited approximately 15 min behind Aqua at a slight horizontal offset, and thus, MLS and AIRS measured the same volume of atmosphere with a time separation of around 8 min. In early 2008, Aura's orbit was changed to allow closer coincidences with CloudSat, and this reduced the separation to around 71 s. Aside from this change, time separation varies minimally.

Routinely paired satellite measurements this close are very unusual. Importantly, their temporal separation is smaller than typical GW dynamical time scales. For example, Wright *et al.* [2011] considered profile pairs within 900 s and 180 km as sufficiently colocated for GW comparisons, while Alexander [2015] accepted profile triplets within 1200 s and 600 km, albeit with mixed results at the wider end of this range.

## 3. Case Study

### 3.1. Description

Figure 1a illustrates colocated AIRS and MLS measurements for AIRS granule 56 of the 6 May 2008. The instruments are traveling approximately southwestward, indicated by the arrow. The thick black lines outline the AIRS granule, while black crosses show temporally coincident MLS profiles. By time shifting our MLS data selection window to 71 s after the AIRS measurement, we can instead select the MLS profiles indicated by the red circles, which lie entirely within the AIRS granule. This produces a perfect geographic collocation to within observational uncertainties.

Figure 1b shows data from the northern two thirds of this collocation. Colors show  $T'_A$  in the horizontal plane and  $T'_M$  in the vertical plane. Some alterations have been made to the data for this figure, only for visual clarity, are as follows:

1. The horizontal plane is shown at 0 km altitude rather than 42 km.
2. Due to fundamentally different instrument sensitivities,  $T'_A \ll T'_M$  and has been scaled tenfold to make the correspondence clearer.
3. Both data sets have been interpolated onto a  $0.33^\circ$  latitude grid ( $\times 0.33^\circ$  longitude for AIRS).
4. Data have been boxcar smoothed by 3 pixels.

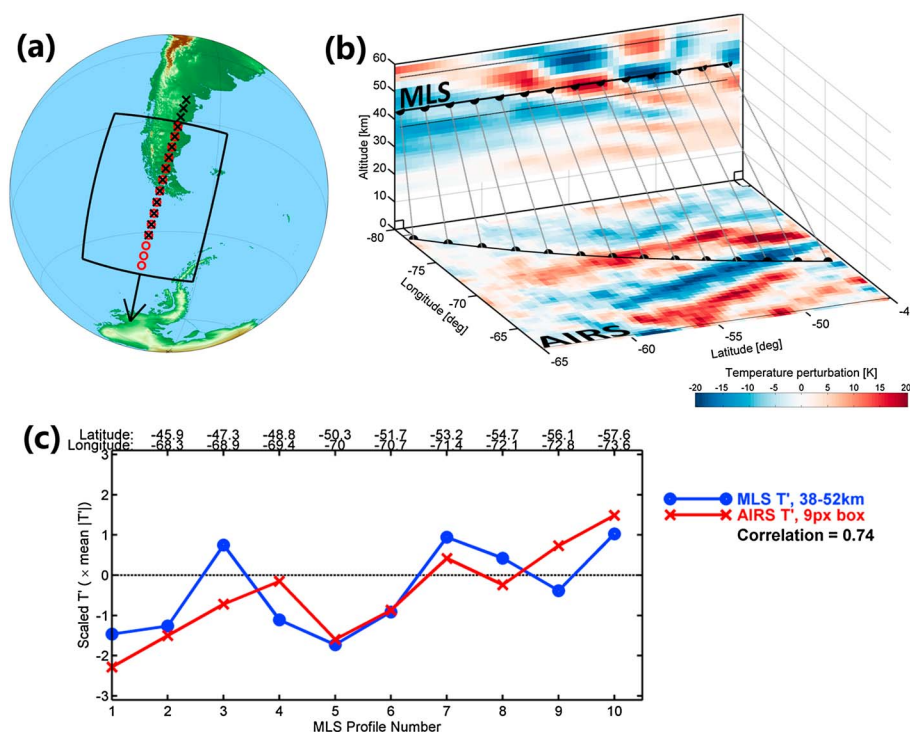


**Figure 1.** (a) Overlap between AIRS and MLS measurements for granule AIRS.2008.05.06.057. Black arrow indicates direction of travel, black solid lines indicate the outline of the AIRS granule, and black crosses indicate temporally coincident MLS profiles. By shifting the time window used to select the MLS data, a precise geographic coincidence can be generated with only a 71 s time difference (red circles). (b) Temperature perturbations  $T'$  from the same pairing, with MLS shown on the vertical plane and AIRS on the horizontal plane. Semicircles indicate identical points (MLS profile locations at 42 km altitude) in both planes. Note that the data have been interpolated and scaled for visual clarity, as described in the text. (c) Along-track series of scaled MLS and AIRS  $T'$  at each MLS profile location, after local spatial averaging to compensate for different weighting functions as described in text.

In the AIRS plane, the curved line shows the path of the MLS scan track. In the MLS plane, thin horizontal lines indicate the approximate FWHM of the AIRS weighting function, with the thick horizontal line showing the dominant altitude. Semicircles indicate MLS profile locations at 42 km altitude. Grey lines link corresponding points.

In both planes, a wavelike signature is visible, manifesting itself as alternating slanted bands of positive and negative  $T'$ . These bands increase in amplitude with height, a typical GW signature due to amplitude growth with falling density. Allowing for the scaled  $T'_{A'}$  values at the same 3-D location, i.e., the semicircle-indicated points, correspond well: in almost all cases, a positive perturbation in one plane corresponds to a positive perturbation in the other, and vice versa. Some points deviate from this slightly but acceptably so allowing for the different background removal, the deep weighting functions, and the temporal offset. The amplitude of this wave in the MLS observations ( $\sim 20$  K or more) initially seems large but is consistent with previous observations over this region with both HIRDLS and AIRS [e.g., Hoffmann and Alexander, 2009, Figure 10].

Figure 1c assesses this match by comparing an along-track series of  $T'_M$  (blue) with one of  $T'_{A'}$  (red).  $T'_M$  have been averaged over the 28–52 km altitude range to better match the vertically deep AIRS weighting functions, while  $T'_{A'}$  have been averaged over a 9 pixel ( $\sim 45$  km each side) box to better match the horizontally broader MLS weighting functions. Both data sets have been scaled by the mean value for that series. We see a 0.74 Pearson linear correlation between these series, which indicates a good match given the large approximations.

From these observations, we assume that (a) we are observing a GW and (b) both instruments see the same GW. Under these assumptions, we are able to characterize the 3-D wave structure, as outlined below. Note that there are several important caveats to this analysis, discussion of which will be deferred to section 5 in order to streamline the methodological description. This combined analysis is thus able to yield information on the horizontal and vertical structure of the observed wave.



### 3.2. Data Preparation, Preprocessing, and Tapering

We first combine the above granule with those immediately preceding and following, to produce a combined three-granule swath (hereafter simply “swath”). This allows us to better detect any GWs crossing the inter-granule boundary and improves spectral resolution in the AT direction. We select MLS data corresponding to this new combined swath rather than the original granule.

We then interpolate  $T'_A$  and  $T'_M$  onto uniform 2-D grids  $T'_{A,i}$  and  $T'_{M,i'}$  to allow spectral analysis. For AIRS, this is a regular grid in AT ( $x_{AT}$ ) and XT ( $x_{XT}$ ) distance, with the spacing defined as the mean in each direction separately. For MLS, we use  $x_{AT}$  as the horizontal coordinate and a uniform 1 km scale  $z_M$  in the vertical over the full vertical range of MLS data. The two data sets share a common AT axis, the black line in Figure 1(b), which in the coordinate frame of the two data sets is a straight line. We define the origin for both as the  $(x_{AT}, x_{XT}, z_M)$  point at 42 km altitude corresponding to the first MLS profile within the swath.

Since MLS will not see waves solely present at large  $|x_{XT}|$  (or AIRS at large  $|z_M|$ ), we taper amplitudes at large distances from the  $(x_{AT}, 0, 0)$  axis. This allows them to contribute to our spectral analysis while preventing them from dominating the amplitude output used later for geolocation. The details of the taper were chosen empirically. For  $T'_{A,i'}$  we apply a factor of 0.90 per 15 km at AT distances more than 300 km from  $x_{AT} = 0$ , while for  $T'_{M,i}$  we scale by 0.80× per 1 km from  $z_M = 0$  at  $|z_M| > 15$  km. This leaves us with the tapered regularly gridded 2-D data sets  $T'_{A,i,t}(x_{AT}, x_{XT})$  and  $T'_{M,i,t}(x_{AT}, z_M)$ .

### 3.3. Spectral Analysis—AIRS

Next, we spectrally analyze our data by using a two-dimensional S-Transform (2DST) technique [Hindley *et al.*, 2016]. We first apply the 2DST to  $T'_{A,i,t}$ . This provides, for each geographic point, an estimate of the amplitude of all AT and XT wave numbers  $k_{AT}$  and  $k_{XT}$  at that point, i.e., a four-dimensional matrix of wave amplitudes  $A_A(x_{AT}, x_{XT}, k_{AT}, k_{XT})$ .

We identify the spectral peak of this matrix by summing over the geographic elements  $(x_{AT}, x_{XT})$  to produce  $A_A(k_{AT}, k_{XT})$ , find the peak of the matrix, and assume that the location of this peak  $(k_{AT,pk}, k_{XT,pk})$  is that of the “dominant” wave present in the granule. To focus our analysis solely on this wave, we discard all matrix elements for wave number combinations other than this, leaving a horizontal-plane geographic amplitude distribution for this dominant wave mode  $A_A(x_{AT}, x_{XT}, k_{AT} = k_{AT,pk}, k_{XT} = k_{XT,pk})$ . Finally, we spatially localize the wave by finding all locations where this value is more than 1 standard deviation above the swath mean.

### 3.4. Spectral Analysis—MLS

We now need to find the corresponding signal in the MLS data. We apply the 2DST to  $T'_{M,i,t}$ , returning the four-dimensional matrix  $A_M(x_{AT}, z_M, k_{AT}, m)$ , where  $m$  is vertical wave number. Since we wish to measure the same wave in both data sets, we then discard all  $k_{AT}$  values that do not equal the already measured  $k_{AT,pk}$ , leaving the three-dimensional matrix  $A_M(x_{AT}, z_M, m)$ . As before, we sum over geographic dimensions and identify the peak in the resulting 1-D distribution. This gives us an estimate for the vertical wave number of the observed wave  $m_{pk}$  and a vertical-plane amplitude distribution  $A_M(x_{AT}, z_M)$ . Crucially,  $m_{pk}$  is a signed quantity, where a positive value indicates a wave aligned with phase fronts descending in the along-track direction and vice versa.

### 3.5. Estimating Geophysical Quantities

Our above analyses directly measure the three-dimensional wave number vector of the dominant wave in the swath  $(k_{AT}, k_{XT}, m)$ . Since the measurements are near instantaneous, the combination  $(k_{AT}, k_{XT})$  is 180° ambiguous, and we define them such that  $k_{XT}$  is signed while  $k_{AT}$  is always positive. Using  $m$ , we break this ambiguity tie by assuming upward propagation of the wave: if we measure a positive value of  $m$ , then we reverse the direction of our wave vector in all three dimensions. We then compute the zonal and meridional wave numbers  $(k, l)$  by rotating  $(k_{AT}, k_{XT})$  into the appropriate latitude/longitude coordinate frame using AIRS geolocation data. This provides a three-dimensional wave vector estimate  $(k, l, m)$  under the assumption of an upward propagating wave. For our example wave, these values are  $(-2.3, 5 \times 10^{-2}, 45) \times 10^{-3} \text{ km}^{-1}$  or in wavelength  $(1/k)$  terms  $(-435, 20,000, 22)$  km. This yields a horizontal wavelength of 435 km and a vertical wavelength of 22 km, which agrees with visual inspection of Figure 1b.

We define the wave amplitude  $T'_W$  as the peak value of  $A_M(x_{AT}, z_M = 0)$ . This value is chosen because (i) MLS has much greater  $T'$  sensitivity than AIRS and (ii) this is a perturbation to a “true” retrieved temperature rather than to a brightness temperature. This provides an amplitude estimate for the single geographic point closest to this peak. We then use AIRS to estimate the geographical extent of this wave. We construct a weighting

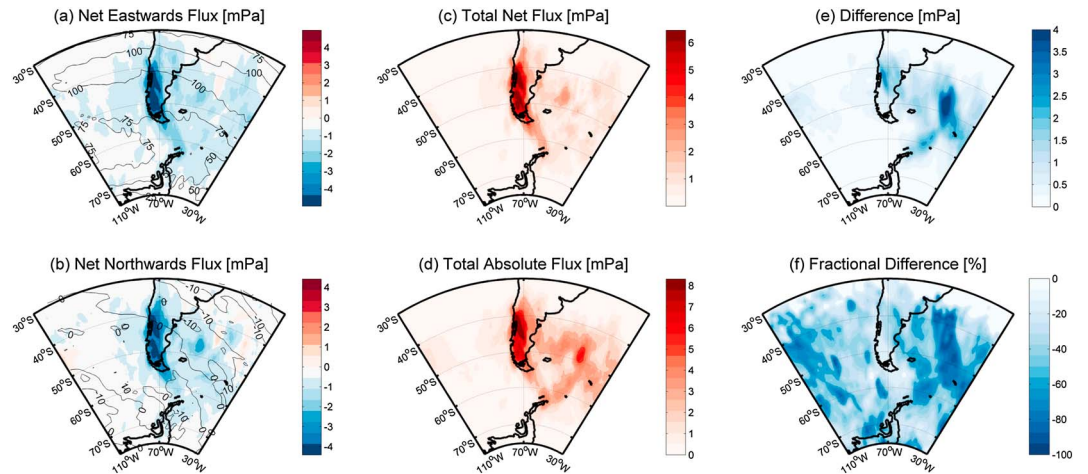


**Figure 2.** Observed momentum fluxes for August 2008 over the Southern Andes/Antarctic Peninsula region. Values are averaged over all AIRS/MLS overpasses, not just those containing observed waves. (a) Net eastward MF. (b) Net northward MF. (c) Net total MF. (d) Total absolute (i.e., nondirectional) MF. (e) Absolute difference  $[F_A - F_N]$ . (f) Fractional difference  $[100 \times (F_A - F_N)/F_A]$ .

matrix in latitude and longitude using  $A_A(x_{AT}, x_{XT})$ , normalized to a value of 1 at the highest-amplitude point along  $(k_{AT}, 0, 0)$ , and scale  $T'_W$  geographically according by this. For our example, the peak value of  $T'_W$  is 1.9 K. Finally, we compute the MF associated with this wave individually for each geographic point in the AIRS swath as [Ern et al., 2004; Alexander et al., 2009]

$$[M_x, M_y] = \frac{\rho}{4\pi} \frac{[k, l]}{|m|} \left(\frac{g}{N}\right)^2 \left(\frac{T'_W}{\bar{T}}\right)^2 \quad (2)$$

where  $M_x$  and  $M_y$  are the zonal and meridional MF, respectively;  $\rho$ ,  $N$ , and  $\bar{T}$  are the local atmospheric density, buoyancy frequency, and MLS-derived background temperature; and  $g$  is the acceleration due to gravity. Equation (2) assumes that the waves are in the midfrequency range  $N \gg \hat{\omega} \gg f$ , which this wave is with an intrinsic frequency  $\sim 0.6 \times 10^{-3} \text{ s}^{-1}$  (equation (23) of Fritts and Alexander [2003]). This is usually true for waves observable by combined AIRS/MLS data. For our example, the peak MF value is  $(-5, 0.1) \text{ mPa}$  in the zonal and meridional directions, respectively, i.e., a near westward flux of 5 mPa.

#### 4. Net Observed Fluxes in the Andes/Antarctic Peninsula Region

We now illustrate our method further by considering fluxes from all waves observed over the southern Andes during August 2008. This region is extremely important wave dynamically [e.g., Eckermann and Preusse, 1999; Jiang et al., 2002; Yan et al., 2010; Sato et al., 2012; Hoffmann et al., 2013; Hindley et al., 2015], and GW activity as observed by AIRS and MLS during this month was not atypical for the season [Wright et al., 2015a].

Specifically, we analyze all AIRS/MLS passes over the region  $75^\circ\text{S} - 30^\circ\text{S}, 110^\circ\text{W} - 30^\circ\text{W}$ . AIRS and MLS passed over at least some part of the region 1039 times during this month. There is a strong coverage bias toward the south, with the number of passes meridionally within 300 km of each geographic location rising from 100 in the northernmost parts of the region to around 400 at the southernmost point. Of these 1039 overpasses, 671 passed the quality control checks of section 5.2 below.

Each swath overlapping the region is individually processed as described above, with any duplicate waves arising from the reuse of a given adjacent granule removed at the final stage of analysis. Specifically, we remove any detected waves with a separation less than  $5^\circ$  in both latitude and longitude in any 30 min period. Measured MFs are gridded onto a  $0.5 \times 0.5^\circ$  grid box latitude-longitude grid and are averaged over all 1039 passes rather than just the 671 containing high-quality waves. Figure 2 shows our results.

##### 4.1. Net Fluxes

First, we consider first net eastward (i.e., zonal) and northward (i.e., meridional) MF, Figures 2a and 2b.

The figures show remarkably finely localized peaks over the southern Andes compared to measurements derived entirely from limb sounders [e.g., Alexander *et al.*, 2008; Preusse *et al.*, 2009; Wright *et al.*, 2010; Yan *et al.*, 2010]. We suggest this reflects near-vertical ascent of orographic waves. This localisation is due to the additional horizontal information provided by AIRS. We can thus clearly distinguish between subregional wave sources.

The largest contribution to the total net MF is from eastern Patagonia, with observed net MF per satellite overpass (hereafter “net flux”) peaking at  $(M_x, M_y) \sim (-5, -4)$  mPa, i.e., net flux of 6.5 mPa in a near southwestward (145° anticlockwise from north) direction. This is consistent with orographic generation from the projection of local surface winds over the southern Andes. This produces waves with a wavevector pointing upwind of the mountain ridge, in this direction. It is also consistent with the austral Spring (October–December) 2005 balloon observations and WRF simulations of Plougonven *et al.* [2013].

This net flux peak, significantly reduced in amplitude, continues southward over the Drake Passage to the tip of the Antarctic Peninsula. Net fluxes here are  $(-2.5, -0.7)$  mPa, i.e., a magnitude of 2 mPa at a direction of 115° anticlockwise from north. This is slightly inconsistent with theoretical expectations and Plougonven *et al.* [2013], from which we would anticipate net fluxes in a northwestward direction. Possible reasons for this difference include the presence of waves from other sources or local details of surface wind direction or higher-level wind filtering.

Finally, we observe patches of high net MF over the open ocean, particularly downstream (east) of the Andes. These may be due to waves traveling from the Andes or incomplete cancelation of nonorographic MF (discussed below).

#### 4.2. Total Absolute Versus Total Net Fluxes

Standard single-satellite GWs observations measure absolute MF, i.e., the directionless magnitude of the observed wave fluxes. The mean of this absolute magnitude is often assumed to be proportional to the net MF. Here we can assess the difference between this absolute estimate and the net estimate produced by our measurements.

Figure 2c shows the total net flux over our region, i.e.,

$$F_N = \frac{1}{P} \sqrt{(\Sigma F_e)^2 + (\Sigma F_n)^2} \quad (3)$$

while Figure 2d shows the total absolute flux, i.e.,

$$F_A = \frac{1}{P} \sqrt{(\Sigma |F_e|)^2 + (\Sigma |F_n|)^2}. \quad (4)$$

Here  $P$  is the number of satellite overpasses at a given location, and  $F_e$  and  $F_n$  are the eastward and northward fluxes associated with each individual pass.  $F_N$  is thus the magnitude of observed net flux at a given location, while  $F_A$  is the magnitude of the observed absolute flux. The difference between these values is the degree to which observed wave fluxes cancel out when added as vectors.

Figures 2(e) and 2(f) show the absolute  $[F_A - F_N]$  and fractional/percentage  $[100 \times (F_A - F_N)/F_A]$  differences between these two values. By definition,  $F_A > F_N$ . Fractional differences are often large,  $>50\%$ . However, the majority of these large fractional differences are associated with regions of low total flux and thus represent only small absolute differences. Over the majority of the large net flux source regions in Patagonia and the tip of the Antarctic Peninsula, fractional differences are smaller,  $\sim 0-25\%$ , and absolute differences are  $< \sim 1$  mPa. There is a small region in northern Patagonia ( $\sim 45^\circ\text{S}$ ,  $\sim 75^\circ\text{W}$ ) with an absolute difference  $> 2$  mPa; but this is an extremely large net flux region, and the fractional difference is small.

Major differences, however, exist in the western and eastern portions of our region, i.e., upstream and (especially) downstream. As expected from previous studies [e.g., Ern *et al.*, 2004; Alexander *et al.*, 2008; Sato *et al.*, 2012], we see significantly more flux downstream (eastward) of the Andes than upstream (westward) in both net and absolute terms. However, there are important differences between the net and the absolute, with differences as large as 4 mPa. A possible reason for these differences could be significant nonorographic MF with a more isotropic directional distribution, perhaps arising due to baroclinic instability [e.g., Hendricks *et al.*, 2014], with large absolute but small net MF by comparison to the orographic flux generated by the Andes.



## 5. Discussion

### 5.1. Methodological Constraints

We have here presented a proof of concept study of our new method for wave detection from the AIRS/MLS instrument pairing. Several methodological biases remain, which future work will resolve. We identify four key issues.

#### 5.1.1. Input Data Consistency

The data sources are currently not ideally matched. Specifically, we use AIRS brightness temperatures and MLS-retrieved mixed temperature and remove large-scale signals from the data sets in different ways. This is to reduce the computational overhead associated with a full retrieval of AIRS temperature at the necessary resolution [e.g., *Hoffmann and Alexander, 2009*], restricting us to use of  $T_b$ . Thus, the background for AIRS must be removed in a manner which compensates for limb brightening [*Alexander and Barnett, 2007*].

Use of such a product would allow consistent planetary wave removal between the two data sets. It would not, however, correct fully for the significant low bias in  $T'_A$ , since this arises at least partially due to weighting function depth, and thus, it would still be appropriate to define  $T'_W$  in terms of the MLS observations. The primary effect of resolving this issue, therefore, would be to reduce the mismatch-induced noise level, allowing the detection of lower amplitude waves. In the region studied here, this is not a major issue due to the large amplitude of most waves.

A related issue is the relative viewing geometry of the observations. AIRS observes data in the nadir, and thus, the 2-D horizontal plane of data is wrapped around the curvature of the Earth. MLS observes in the limb, with a 2-D plane of vertical data curved in a subtly different way relative to the surface. This effect is very small relative to the mismatch between weighting functions and thus will not significantly affect our results.

#### 5.1.2. Low Estimated Wave Amplitudes

$T'_W$  for our example wave is much smaller than would be expected from Figure 1. This is a consistent issue across all data examined.

Part of this effect arises from selecting a single mode of the 2DST, which in common with the 1D-ST and other spectral methods underestimates wave amplitudes to a large degree [*Stockwell et al., 1996; Wright et al., 2015b; Hindley et al., 2016*]. This is due to the part of the geophysical signal being spread over other frequencies. Thus, our results are low biased.

A more important contributor is the tapering applied to force waves to be detected near to the  $(x_{AT}, 0, 0)$  axis. This significantly reduces the amplitude of the wave modes fitted to the data overall and is the cause of most of the amplitude reduction observed.

Resolution of both these issues will require a different spectral technique, likely requiring some trade-off, for example, reduced spectral or geographic localisation.

#### 5.1.3. Spectral Feature Selection

Our method selects the single spectral feature in each swath with the largest contribution to the geographic sum of  $A_A$ . This implicitly biases our results to waves with large spatial extent and to waves which lie along the  $(x_{AT}, 0, 0)$  axis, both of which will contribute to many geographic points. These waves on average are likely to have long horizontal wavelengths, and thus carry much less MF than smaller scale and shorter horizontal wavelength waves, which are potentially accessible to the AIRS/MLS combination.

Our method also limits us to detecting a single wave from each swath. A better solution will be to fully process the four-dimensional matrix  $A_A$  for all strong wave signals and process these individually.

#### 5.1.4. Assumption of Vertical Ascent

To compute the full three-dimensional wave vector, we assume that waves upwardly propagate. This assumption is very reasonable in the context of the current study. This region in this season is dominated by a known major orographic wave source, and both wave-resolving model *Sato et al. [2012]* and ray-tracing [*Preusse et al., 2002*] studies confirm this. In particular, *Sato et al. [2012]* suggested less than 10% of waves energy in this region was downwardly propagating. Most major nonorographic sources in this region, such as storm tracks [e.g., *Hoskins and Hodges, 2005*], baroclinic growth [e.g., *Hendricks et al., 2014*], and the breakdown of the stratospheric vortex (not relevant in the season studied) are likely to lie well below the 40 km altitude of our analysis and would thus only be detected while traveling upward.

## 5.2. Quality Control and Proportion of Useful Data

We have automatically discarded all swaths for which (a)  $k_{AT}$  is greater than that detectable by MLS ( $\sim > 1/200$  km), (b) the peak value of  $A_M < 1$  K, or (c) the peak value of  $A_A < 0.2$  K. We apply a visual check to all swaths to ensure that (a) the AIRS-derived peak region is geographically well localized and crosses the MLS scan region and (b) a clear wavelike signal of the correct  $k_{AT}$  is visible in the raw MLS data.

Of the 1040 swaths studied for this paper, approximately 20% fail the automated checks, with a further 20% failing the visual inspection. These failure rates, particularly the former, could be reduced by resolving the issues outlined in section 5.1. However, the swaths studied are all in a known region and season of high GW activity, and thus, the fraction of swaths containing useful detectable waves is likely to be a much lower fraction of the total combined data set.

## 6. Conclusions

Our results show that combined AIRS and MLS observations can resolve GWs in 3-D. AIRS data allow accurate characterization of wave properties in the horizontal plane with high geographic localisation, while coincident MLS data directly measure vertical properties. This allows estimation of the wave vertical wavelength and hence MF without necessitating the limiting assumption of an orographic source [e.g., Alexander *et al.*, 2009; Alexander and Grimsdell, 2013]. Combined AIRS/MLS analyses can thus characterize nonorographic MF with the high horizontal resolution available to AIRS and similar hyperspectral sounders. In trade-off, our results are restricted to only the portion of the AIRS scan track close to the MLS scan track and to the portion of the MLS scan track at a similar altitude to an AIRS measurement.

Combined AIRS/MLS data can, in principle, resolve GWs with a vertical wavelength greater than  $\sim 12$  km, subject to the precise weighting function of the AIRS channel used [see, e.g., Wright *et al.*, 2015a, Figure 1]. In the horizontal, the resolution is a function of the angle  $\Delta\theta$  between the wave vector and the MLS scan track, with a minimum resolvable horizontal wavelength  $\lambda_{h,r} = \lambda_h / \cos(\Delta\theta) > \sim 200$  km. This part of the spectrum is believed to carry the majority of GW MF [e.g., Fritts and Alexander, 2003; Ern *et al.*, 2004] and is thus of great geophysical importance.

Furthermore, subject to a tie-breaking assumption—here that the waves propagate upward—paired AIRS/MLS observations can constrain the full three-dimensional direction of the observed waves. This allows the direct computation of net directional MFs, a vital geophysical quantity previously inaccessible to satellite observations. Our example analysis suggests that in the region downstream of the Andes in August, this lack of directional information may lead other analytical methods to significantly overestimate net MF in our spectral region and thus the magnitude of GW drag. This highlights the advantages of our new method.

Future work is necessary to refine this instrument pairing to where it can be usefully applied in bulk to the entire combined AIRS/MLS data set of greater than 1 million AIRS granules. Nevertheless, our work suggests that particularly if these issues are resolved, combined AIRS/MLS measurements will be able to make a vital contribution to addressing the critical need for global resolved net MF estimates in the terrestrial atmosphere.

## Acknowledgments

C.J.W. and N.J.M. are funded by NERC grant NE/K015117/1 and N.P.H. by a NERC PhD studentship awarded to the University of Bath. The authors would also like to acknowledge the AIRS and MLS instrument teams for many years of hard work producing the data sets studied, Eleanor Denham and Andrew Moss for useful discussions related to the analysis method, and Peter Preusse and the NERC SG-WEX project team for their useful discussions relating to the feasibility of the concept.

## References

- Alexander, M. J. (2015), Global and seasonal variations in three-dimensional gravity wave momentum flux from satellite limb sounding temperatures, *Geophys. Res. Lett.*, *42*, 6860–6867, doi:10.1002/2015GL065234.
- Alexander, M. J., and C. Barnet (2007), Using satellite observations to constrain parameterizations of gravity wave effects for global models, *J. Atmos. Sci.*, *64*(5), 1652–1665, doi:10.1175/JAS3897.1.
- Alexander, M. J., and A. W. Grimsdell (2013), Seasonal cycle of orographic gravity wave occurrence above small islands in the Southern Hemisphere: Implications for effects on the general circulation, *J. Geophys. Res. Atmos.*, *118*, 11,589–11,599, doi:10.1002/2013JD020526.
- Alexander, M. J., and H. Teitelbaum (2011), Three-dimensional properties of Andes mountain waves observed by satellite: A case study, *J. Geophys. Res.*, *116*, D23110, doi:10.1029/2011JD016151.
- Alexander, M. J., et al. (2008), Global estimates of gravity wave momentum flux from High Resolution Dynamics Limb Sounder (HIRDLS) observations, *J. Geophys. Res.*, *113*, D15S18, doi:10.1029/2007JD008807.
- Alexander, M. J., S. D. Eckermann, D. Broutman, and J. Ma (2009), Momentum flux estimates for South Georgia Island mountain waves in the stratosphere observed via satellite, *Geophys. Res. Lett.*, *36*, L12816, doi:10.1029/2009GL038587.
- Alexander, M. J., et al. (2010), Recent developments in gravity-wave effects in climate models and the global distribution of gravity-wave momentum flux from observations and models, *Q. J. R. Meteorol. Soc.*, *136*(650), 1103–1124, doi:10.1002/qj.637.
- Andrews, D. G., J. R. Holton, and C. B. Leovy (1987), *Middle Atmosphere Dynamics*, Int. Geophys. Ser., vol. 40, Academic Press, San Diego, Calif.
- Aumann, H. H., et al. (2003), AIRS/AMSU/HSB on the aqua mission: Design, science objectives, data products, and processing systems, *IEEE Trans. Geosci. Remote Sens.*, *41*, 253–263, doi:10.1109/TGRS.2002.808356.
- Barnett, J. J., C. L. Hepplewhite, S. M. Osprey, J. C. Gille, and R. Khosravi (2008), Cross-validation of HIRDLS and COSMIC radio-occultation retrievals, particularly in relation to fine vertical structure, *Proc. SPIE*, *7082*, 708216, doi:10.1117/12.800702.

- Chahine, M. T., et al. (2006), AIRS: Improving weather forecasting and providing new data on greenhouse gases, *Bull. Am. Meteorol. Soc.*, 87(7), 911–926, doi:10.1175/BAMS-87-7-911.
- Eckermann, S. D., and P. Preusse (1999), Global measurements of stratospheric mountain waves from space, *Science*, 286(5444), 1534–1537.
- Ern, M., P. Preusse, M. J. Alexander, and C. D. Warner (2004), Absolute values of gravity wave momentum flux derived from satellite data, *J. Geophys. Res.*, 109, D20103, doi:10.1029/2004JD004752.
- Faber, A., P. Llamedo, T. Schmidt, A. De La Torre, and J. Wickert (2013), On the determination of gravity wave momentum flux from GPS radio occultation data, *Atmos. Meas. Tech.*, 6(11), 3169–3180, doi:10.5194/amt-6-3169-2013.
- Fritts, D. C. (1984), Gravity wave saturation in the middle atmosphere: A review of theory and observations, *Rev. Geophys.*, 22(3), 275–308, doi:10.1029/RG022i003p00275.
- Fritts, D. C., and M. J. Alexander (2003), Gravity wave dynamics and effects in the middle atmosphere, *Rev. Geophys.*, 41(1), 1003, doi:10.1029/2001RG000106.
- Hendricks, E. A., J. D. Doyle, S. D. Eckermann, Q. Jiang, and P. A. Reinecke (2014), What is the source of the stratospheric gravity wave belt in austral winter?, *J. Atmos. Sci.*, 71(5), 1583–1592, doi:10.1175/JAS-D-13-0332.1.
- Hindley, N. P., C. J. Wright, N. D. Smith, and N. J. Mitchell (2015), The southern stratospheric gravity wave hot spot: Individual waves and their momentum fluxes measured by COSMIC GPS-RO, *Atmos. Chem. Phys.*, 15(14), 7797–7818, doi:10.5194/acp-15-7797-2015.
- Hindley, N. P., N. D. Smith, C. J. Wright, and N. J. Mitchell (2016), A two-dimensional stockwell transform for gravity wave analysis of AIRS measurements, *Atmos. Meas. Tech. Discuss.*, doi:10.5194/amt-2015-383, in press.
- Hoffmann, L., and M. J. Alexander (2009), Retrieval of stratospheric temperatures from Atmospheric Infrared Sounder radiance measurements for gravity wave studies, *J. Geophys. Res.*, 114, D07105, doi:10.1029/2008JD011241.
- Hoffmann, L., X. Xue, and M. J. Alexander (2013), A global view of stratospheric gravity wave hotspots located with atmospheric infrared sounder observations, *J. Geophys. Res. Atmos.*, 118, 416–434, doi:10.1029/2012JD018658.
- Hoffmann, L., M. J. Alexander, C. Clerbaux, A. W. Grimsdell, C. I. Meyer, T. Rößler, and B. Tournier (2014), Intercomparison of stratospheric gravity wave observations with AIRS and IASI, *Atmos. Meas. Tech. Discuss.*, 7(8), 8415–8464, doi:10.5194/amt-7-8415-2014.
- Holton, J. R. (1983), The influence of gravity wave breaking on the general circulation of the middle atmosphere, *J. Atmos. Sci.*, 40, 2497–2507.
- Hoskins, B. J., and K. I. Hodges (2005), A new perspective on Southern Hemisphere storm tracks, *J. Clim.*, 18(20), 4108–4129, doi:10.1175/JCLI3570.1.
- Jiang, J. H., D. L. Wu, S. D. Eckermann, and J. Ma (2002), Upper Atmosphere Research Satellite (UARS) MLS observation of mountain waves over the Andes, *J. Geophys. Res.*, 107(D20), 8273, doi:10.1029/2002JD002091.
- Lindzen, R. S. (1981), Turbulence and stress owing to gravity wave and tidal breakdown, *J. Geophys. Res.*, 86(C10), 9707–9714.
- Livesey, N. J., et al. (2013), *Earth Observing System (EOS) Aura Microwave Limb Sounder (MLS) Data Quality and Description, Version 3.3 and 3.4*, NASA Jet Propul. Lab., Pasadena, Calif.
- Olsen, E. T., E. Fishbein, S. Granger, S.-Y. Lee, E. Manning, M. Weiler, J. Blaisdell, and J. Susskind (2007), *AIRS/AMSU/HSB Version 5 Data Release User Guide*, Jet Propulsion Lab., California Inst. of Technol., Pasadena, Calif.
- Plougonven, R., A. Hertzog, and L. Guez (2013), Gravity waves over Antarctica and the Southern Ocean: Consistent momentum fluxes in mesoscale simulations and stratospheric balloon observations, *Q. J. R. Meteorol. Soc.*, 139(670), 101–118, doi:10.1002/qj.1965.
- Preusse, P., A. Dörnbrack, S. D. Eckermann, M. Riese, B. Schaeler, J. T. Bacmeister, D. Broutman, and K. U. Grossman (2002), Space-based measurements of stratospheric mountain waves by CRISTA 1. Sensitivity, analysis method, and a case study, *J. Geophys. Res.*, 107(D23), 8178, doi:10.1029/2001JD000699.
- Preusse, P., S. D. Eckermann, M. Ern, J. Oberheide, R. H. Picard, R. G. Roble, M. Riese, J. M. R. Iii, and M. G. Mlynarczyk (2009), Global ray tracing simulations of the SABER gravity wave climatology, *J. Geophys. Res.*, 114, D08126, doi:10.1029/2008JD011214.
- Sato, K., S. Tatenos, S. Watanabe, and Y. Kawatani (2012), Gravity wave characteristics in the Southern Hemisphere revealed by a high-resolution middle-atmosphere general circulation model, *J. Atmos. Sci.*, 69(4), 1378–1396, doi:10.1175/JAS-D-11-0101.1.
- Schoeberl, M. R., et al. (2006), Overview of the EOS Aura mission, *IEEE Trans. Geosci. Remote Sens.*, 44(5), 1066–1074, doi:10.1109/TGRS.2005.861950.
- Stockwell, R. G., L. Mansinha, and R. Lowe (1996), Localization of the complex spectrum: The S transform, *IEEE Trans. Signal Process.*, 44(4), 998–1001, doi:10.1109/78.492555.
- Wang, L., and M. J. Alexander (2010), Global estimates of gravity wave parameters from GPS radio occultation temperature data, *J. Geophys. Res.*, 115, D21122, doi:10.1029/2010JD013860.
- Waters, J. W., et al. (2006), The Earth Observing System Microwave Limb Sounder (EOS MLS) on the aura satellite, *IEEE Trans. Geosci. Remote Sens.*, 44(5), 1075–1092, doi:10.1109/TGRS.2006.873771.
- Wright, C. J. (2010), Stratospheric gravity waves measurements using HIRDLS data, Dphil (phd) thesis, Univ. of Oxford, Oxford.
- Wright, C. J., S. M. Osprey, J. J. Barnett, L. J. Gray, and J. C. Gille (2010), High resolution dynamics limb sounder measurements of gravity wave activity in the 2006 Arctic stratosphere, *J. Geophys. Res.*, 115, D02105, doi:10.1029/2009JD011858.
- Wright, C. J., M. Belmonte Rivas, and J. C. Gille (2011), Intercomparisons of HIRDLS, COSMIC and SABER for the detection of stratospheric gravity waves, *Atmos. Meas. Tech.*, 4(8), 1581–1591, doi:10.5194/amt-4-1581-2011.
- Wright, C. J., N. P. Hindley, A. C. Moss, and N. J. Mitchell (2015a), Multi-instrument gravity-wave measurements over Tierra del Fuego and the Drake Passage—Part 1: Potential energies and vertical wavelenghts from AIRS, COSMIC, HIRDLS, MLS-Aura, SAAMER, SABER and radiosondes, *Atmos. Meas. Tech. Discuss.*, 8(7), 6797–6876, doi:10.5194/amt-8-6797-2015.
- Wright, C. J., S. M. Osprey, and J. C. Gille (2015b), Global distributions of overlapping gravity waves in HIRDLS data, *Atmos. Chem. Phys.*, 15(4), 4333–4382, doi:10.5194/acpd-15-4333-2015.
- Wu, D. L., and J. W. Waters (1996), Satellite observations of atmospheric variances: A possible indication of gravity waves, *Geophys. Res. Lett.*, 23(24), 3631–3634, doi:10.1029/96GL02907.
- Yan, X., N. Arnold, and J. Remedios (2010), Global observations of gravity waves from high resolution dynamics limb sounder temperature measurements: A yearlong record of temperature amplitude and vertical wavelength, *J. Geophys. Res.*, 115, D10113, doi:10.1029/2008JD011511.